Rare Met. (2017) 36(12):951–961
DOI 10.1007/s12598-016-0830-4

RARE METALS
www.editorialmanager.com/rmet

Microstructure and grain boundary morphology evolution of a novel Co–9Al–9W–2Ta–0.02B alloy doped with yttrium

Jian-Qiang Ma, Fei Zhong, Shu-Suo Li, Jiang-Bo Sha*

Received: 26 October 2015 / Revised: 24 November 2015 / Accepted: 9 November 2016 / Published online: 17 March 2017
© The Nonferrous Metals Society of China and Springer-Verlag Berlin Heidelberg 2017

Abstract The microstructures and grain boundary morphologies of a novel Co–9Al–9W–2Ta–0.02B alloy doped with yttrium (Y) (0.01, 0.05, 0.10, and 0.20; at%) were investigated as functions of aging temperatures (900 and 1000 °C) and time (50 and 150 h). The aged alloys all exhibit a γ/γ'-Co_3(Al, W) coherent microstructure in grain interiors, whereas an intermetallic κ-Co_3(W) phase precipitates at grain boundaries. Y is found to fully segregate at grain boundaries and changes grain boundary precipitate morphologies. For 0.01Y alloy, bright κ-Co_3(W) stripes precipitate along grain boundaries, where a needlelike κ-Co_3(W) phase grows from grain boundaries or κ-Co_3(W) stripes toward grain interior. As the nominal Y content increases, the stripe and needlelike κ-Co_3(W) precipitates at grain boundaries are strongly restrained and disappear in 0.20Y alloy, leaving fine κ-Co_3(W) particles scattered at grain boundaries. It is noted that more Y segregation may increase the number of low-angle grain boundaries (LABs, with misorientations of <15°), whereas it eliminates O impurities from grain boundaries. Finally, the effect of Y segregation on tensile behavior of Co–Al–W–Ta–B alloy was discussed from the viewpoints of grain boundary precipitate morphologies, grain boundary character distribution (GBCD), and impurity segregation.

Keywords Intermetallics; Alloy design; Grain boundary segregation; Casting; Microstructure

J.-Q. Ma, F. Zhong, S.-S. Li, J.-B. Sha*
School of Materials Science and Engineering, Beihang University, Beijing 100191, China
e-mail: jbsha@sina.com

1 Introduction

It is well known that conventional Co-based superalloys have a microstructure consisting of a Co sold solution (Co_{SS}) and various carbides. Therefore, the solid-solution hardened Co_{SS} and stiff carbides supply the strength and creep resistance at elevated temperatures [1]. Unfortunately, these two strengthening mechanisms are insufficient at providing high-temperature strength required of conventional Co-based superalloys compared to Ni-based superalloys, which are mainly strengthened by intermetallic γ'-Ni_3Al precipitates and coherent interface of γ/γ' microstructure [2, 3]. An intermetallic γ'-Co_3(Al, W) precipitate [4] discovered in Co–Al–W-based alloys introduces a strong precipitate and coherent strengthening effect and improves the high-temperature strength to a level that is considerably greater than that of conventional Co-based alloys by 50%–100% [5–7] (for example, Haynes188 and Alloy 255), which are strengthened by solid-solution elements and carbides (such as $Cr_{23}C_6$ and Mo_6C) [1].

To increase the stability of γ'-Co_3(Al, W) phase and the strength both at room and high temperatures, alloying elements, such as Ta, Cr, Ti, Nb, B and/or Re, and Mo [5–14], are frequently added to Co–Al–W ternary. Systemic research using compressive loading has revealed that Ta is the most efficient strengthening element for a Co–Al–W ternary alloy [5–7, 14]. An addition of 2 at% Ta increases the solvus temperature of γ' phase in Co–9Al–9W alloy from 1000 to 1079 °C and the compressive strength at 800 °C from 360 to 580 MPa [5–7] (this value is only ~300 MPa for conventional Co-based alloys [2, 7]). In addition, strengthening grain boundaries by precipitates of borides or intermetallic phases has been found to be crucial to the compressive creep resistance of

γ'-strengthened Co-based superalloys [11, 12], which have exhibited even better creep strength than the comparable Ni-based alloy IN100.

Co–Al–W alloys are found to exhibit flow stress anomalies at above 600 °C. This dislocation movement mode of the flow stress anomalies in Co–Al–W-based alloys is the same as that found in a γ'-Ni_3Al compound [15, 16]: a slipping of paired 1/2 < 1 1 0 > superpartial dislocations on {0 0 1} planes in addition to {1 1 1} planes in γ' precipitates [5, 6, 17], resulting in flow stress anomalies at 700–800 °C. Recently, studies on tensile behavior of Co–Al–W-based alloys revealed that an elongation of >10% was obtained at room temperature in Co–9.2Al–9.5W [5] and Co–9Al–(5–9)W–2Ta–(0–4)Mo [18] alloys when doped with 0.02 at% B. This mechanism of ductility enhancement is explained by the suppression of intergranular fractures using B, which has been discovered in Ni_3Al single-phase polycrystalline alloys with brittle behavior and grain boundary failure [16]. However, the Co–Al–W-based alloys with B additions exhibit an intergranular cleavage-dominant failure at high temperatures, resulting in tensile plasticity anomalies [19].

In this study, yttrium (Y) was employed as alloying element in a novel Co–9Al–9W–2Ta–0.02B composition. It is expected that Y will segregate at grain boundaries and affect the microstructure, particularly the precipitate morphologies at grain boundaries, which will subsequently alter the tensile failure mode of Co–Al–W-based alloys from intergranular to transgranular fractures at high temperatures. However, to date, an understanding of how Y affects microstructural evolution of Co–Al–W-based alloys is still lacking. A detailed investigation with regard to the microstructural evolution of Co–9Al–9W–2Ta–0.02B–xY alloys was performed with particular attention paid to the aging parameters (temperature and time).

2 Experimental

Button ingots of Co–9Al–9W–2Ta–0.02B–xY alloys ($x = 0.01$, 0.05, 0.10, and 0.20; at%; hereafter referred to as 0.01Y, 0.05Y, 0.10Y, and 0.20Y alloys, respectively), each with a mass of 100 g, were prepared by arc melting in five or six cycles in an argon atmosphere. The purity of all of the raw elements was 99.95 wt% or higher. The ingots were solution-treated at 1350 °C for 8 h in a vacuum, followed by quenching, and then were sealed in an evacuated quartz capsule backfilled with argon. The aging temperatures were 900 and 1000 °C. For each aging temperature, two batches of the four alloys were aged for 50 and 150 h, respectively, before cooling in water. X-ray diffractometer (XRD, Rigaku D/Max 2500PC) was performed on the bulk samples to identify the phase constitution using Cu Kα ($\lambda = 0.15405$ nm) radiation at 40 kV and 40 mA. Backscattered electron (BSE) images were taken to investigate the microstructures of as-cast samples and aged samples using an SEM (Quant 200F). The grain sizes and phase area fractions were statistically determined by quantitative metallographic analysis of the microstructure images taken in BSE mode, and the phase compositions were determined using energy-dispersive X-ray spectroscopy (EDX, Oxford Instruments, UK). The misorientations of the grain boundaries were measured from a crystal orientation map using electron backscattering diffraction (EBSD) with scanning step sizes of 1–3 μm. Electron diffraction patterns of the selected area (SAED) and EDX spectra were obtained using transmission electron microscope (TEM, FEI Tecnai G^2 F20), to confirm the phase crystal structure and composition, respectively. TEM samples with 0.5 mm in thickness were cut and then mechanically ground/thinned to 50 μm. Foils with 3 mm in diameter were obtained from the mechanically thinned samples by punching and then thinned using a GL-696F ion-milled instrument at an angle of 20°, with a voltage of 6 kV and a current of 0.15 mA applied to perforate the samples. Finally, the perforated foils were ion-milled again for 30–40 min at an angle of 15° to remove residual contamination and/or to ameliorate differential thinning effects.

3 Results

3.1 Microstructure of as-cast alloys

The representative SEM images of as-cast 0.01Y, 0.05Y, 0.10Y, and 0.20Y alloys are shown in Fig. 1. The four as-cast alloys exhibit similar microstructures, in which two contrasting zones are observed: a gray matrix and a bright phase. EDX data in Table 1 and phase analysis of Y-free Co–9Al–9W–2Ta–0.02B alloy [19] reveal that the bright phase is an intermetallic Co_3(Ta, Me) with a C15 structure [20], and the Co_3(Ta, Me) content of the four samples falls into a range from 11 vol% to 13 vol%. The gray matrix possesses a dendritic-like morphology (Fig. 1a–d), whereas the bright Co_3(Ta, Me) phase exhibits dot-like or short chin-like morphologies that are distributed within the interdendritic regions of the matrix (Fig. 1a′–d′). To identify the matrix structure, SAED patterns using a beam direction parallel to [0 1 1] $L1_2$ and TEM images were taken from as-cast 0.01Y and 0.20Y alloys, as shown in insets in Fig. 1a′, d′. A two-phase γ-Co_{SS}/γ'-Co_3(Al, W) microstructure is observed in the gray matrix, and a coherent relationship between γ and γ' phases is confirmed by the typically SAED patterns [4]. Insets in Fig. 1a′, d′ show that the regular γ'-Co_3(Al, W) cubes uniformly

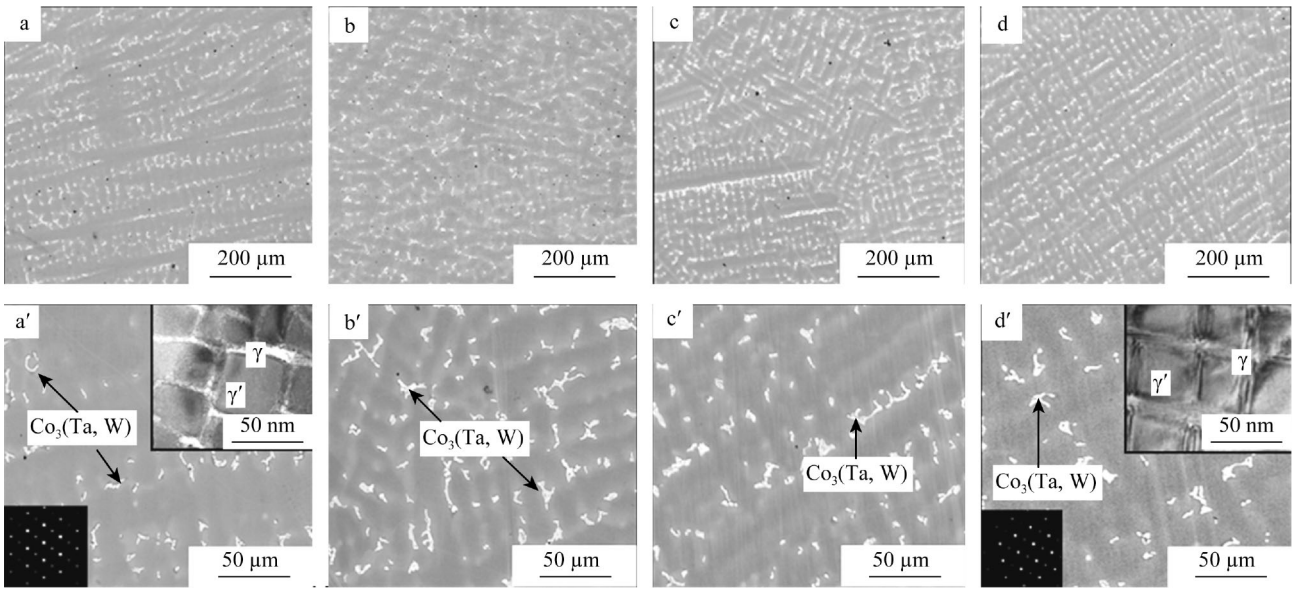

Fig. 1 SEM images of as-cast Y-doped Co–Al–W-based alloys (insets in **a′** and **d′** being TEM representations of γ/γ′ microstructure of gray matrix and typical SAED patterns of γ/γ′ microstructure with beam [0 1 1] $L1_2$: **a**, **a′** 0.01Y alloy, **b**, **b′** 0.05Y alloy, **c**, **c′** 0.10Y alloy, and **d**, **d′** 0.20Y alloy

Table 1 Phase compositions of four as-cast alloys (at%)

Alloys	Phases	Co	Al	W	Ta	Y
0.01Y	Co_3(Ta, W)	70.3	4.4	11.9	13.3	0.1
	γ/γ′ matrix	81.1	8.7	9.6	0.6	–
0.05Y	Co_3(Ta, W)	69.8	3.1	12.4	14.1	0.6
	γ/γ′ matrix	82.1	8.1	9.1	0.7	–
0.10Y	Co_3(Ta, W)	70.5	3.9	11.2	13.2	1.2
	γ/γ′ matrix	82.5	7.8	8.9	0.8	–
0.20Y	Co_3(Ta, W)	69.8	4.5	10.9	12.9	1.9
	γ/γ′ matrix	82.1	8.2	9.2	0.5	–

precipitate in γ-Co_{SS} matrix during solidification, in which γ-Co_{SS} matrix retains a channel-like morphology. Most of the cuboidal γ′ precipitates are <50 nm in length from the cube edges, and the γ channel is 5–10 nm in width. These findings determine that as-cast Co–9Al–9 W–2Ta–0.02B–*x*Y alloys consist of γ, γ′-Co_3(Al, W), and Co_3(Ta, Me) phases.

Table 1 shows phase compositions of as-cast samples. EDX analysis demonstrates that in as-cast samples, Ta partitions to Co_3(Ta, Me) phase rather than γ/γ′ matrix. However, the opposite occurs with Al. In Co–Al–W-based alloys, the segregation behavior of Y is first determined; Y fully segregates in Co_3(Ta, Me) phase, whereas no Y is detected in γ/γ′ matrix. As the nominal Y amount changes from 0.01 at% to 0.20 at%, Y concentration in Co_3(Ta, Me) phase increases from 0.1 at% to 1.9 at%. Because Co_3(Ta, Me) phase exists in the interstices of dendritic-like matrix of as-cast samples, this type of Y distribution may be defined as interdendritic segregation in this work.

3.2 Microstructures of four alloys aged at 900 °C

Figure 2 shows SEM images of the four alloys aged at 900 °C for 50 h. From Fig. 2, it can be observed that significant changes in the phase morphology occur in four aged samples compared to the corresponding as-cast samples. In aged samples, Co_3(Ta, W) phase existing in as-cast samples disappears and equiaxed-like or polygon grains with clear boundaries are observed in the lower magnification images (Fig. 2a–d). The sizes of most of the grains in aged 0.01Y and 0.05Y samples are in the range of 1.0–1.5 mm, while those for 0.10Y and 0.20Y alloys are <1 mm. In grain interiors, a γ/γ′ microstructure is confirmed, in which regular cuboidal γ′-Co_3(Al, W) particles precipitate in γ-Co_{SS} matrix, as observed in SEM and TEM images in Fig. 2a′–d′. The typical SAED patterns of γ/γ′ microstructures of 0.01Y and 0.20Y alloys with the beam [0 1 1] $L1_2$ exhibit a coherent relationship existing between γ and γ′ phases, as shown in insets in Fig. 2a′, d′. At grain boundaries, the morphologies that are similar to those observed in aged multi-component Co–Al–W–(Ta, B, Mo, Ti, Nb, Si) alloys [12] change considerably with the nominal Y contents. The enlarged SEM images in Fig. 2a″, b″ show gray grain boundary morphologies of aged 0.01Y and 0.05Y samples. Two types of bright precipitates are present at gray boundaries: strip-like and needlelike

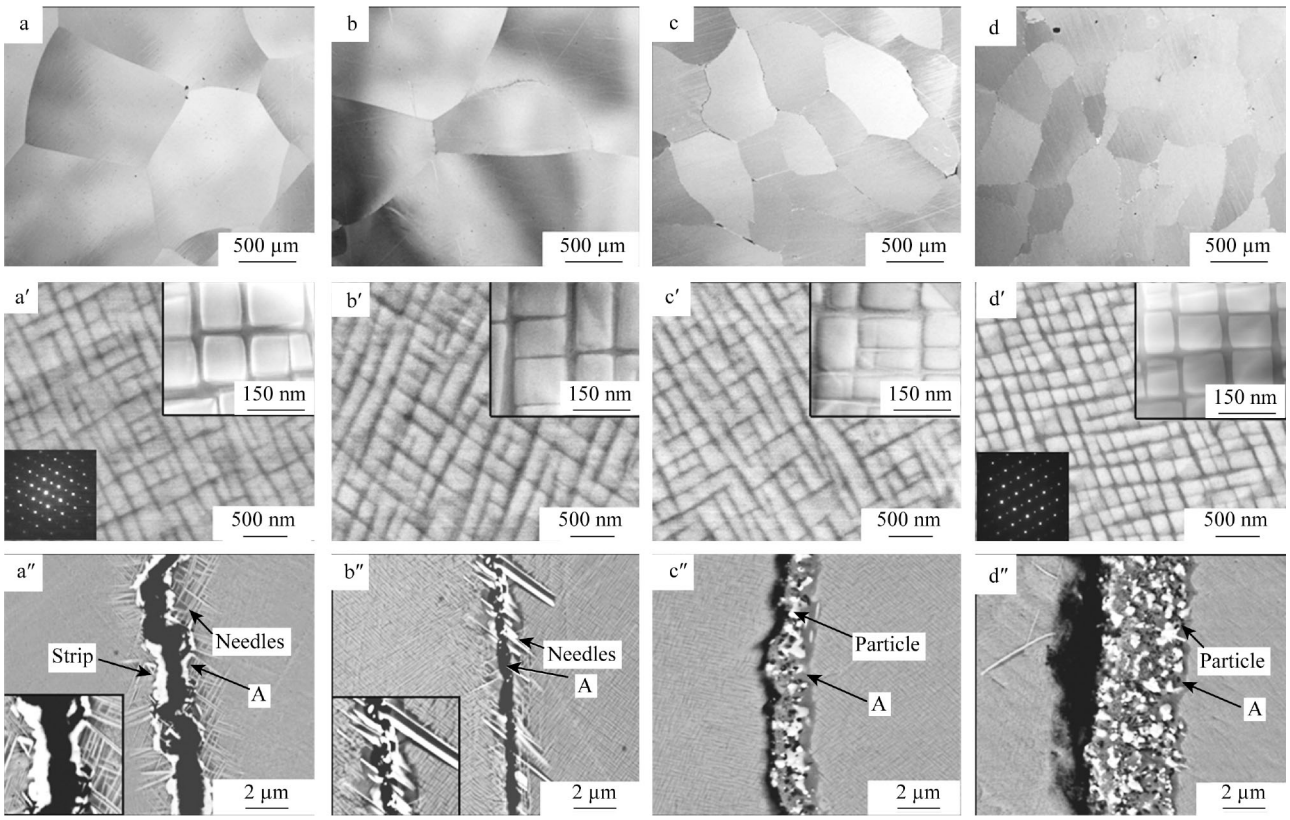

Fig. 2 SEM images of **a–d** macrostructures, **a′–d′** grain interior and **a″–d″** grain boundary of Y-doped Co–Al–W-based alloys aged at 900 °C for 50 h (insets in **a′** and **d′** being TEM representations of γ/γ′ microstructure and typical SAED patterns of γ/γ′ microstructure with beam [0 1 1] $L1_2$: **a, a′, a″** 0.01Y alloy, **b, b′, b″** 0.05Y alloy, **c, c′, c″** 0.10Y alloy, and **d, d′, d″** 0.20Y alloy

precipitates. For the 0.01Y alloy, the bright stripes precipitate along two sides of the grain boundaries and the needles occur inside the grain and adhere the bright stripes and/or grain boundaries (Fig. 2a″). For 0.05Y alloy, only needlelike precipitates growing from the grain boundaries are seen (Fig. 2b″). As Y content increases to 0.10 at% and 0.20 at%, fine bright particles disperse at grain boundaries (Fig. 2c″, d″), and the boundaries of 0.20Y alloy becomes thicker compared to those of other three alloys.

When aged for 150 h, the alloys still exhibit a γ/γ′ coherent microstructure in grain interiors; however, the size of γ′ phase increases, as shown when comparing Fig. 3a–d to Fig. 2a′–d′. At grain boundaries of 0.01Y alloy, the bright stripes along two sides of grain boundaries become coarsen, and denser and longer needle precipitates are present (Fig. 3a′). The needle precipitates are 40–70 nm in width and develop toward grain interiors along two directions with cross-angles of approximately 50°–75° (Fig. 3a′). Careful observations in Fig. 3a′ show that the needles may grow epitaxially from bright stripes or independently from grain boundaries, which indirectly reveals the same phase adopted by needles and stripes at grain boundaries. These two growth mechanisms of needle in 0.01Y alloy are further recognized in the 0.05Y alloy (Fig. 3b′). As nominal Y content increases to 0.10 at%, a tiny amount of bright particles and needles are seen (Fig. 3c′). No needles are present near grain boundaries in 0.20Y alloy. Apparently, bright particles at grain boundaries after aging for 150 h grow (Fig. 3d′) compared to those in 0.20Y sample aged for 50 h (Fig. 2d″).

EDX data in Table 2 reveal that the compositions of γ′ and γ phases in grain interiors of the four aged alloys are almost independent of nominal Y contents and aging time. They are represented by the ranges of (74.5–76.9)Co–(10.5–11.9)Al–(9.8–11.9)W–(2.2–3.3)Ta and (78.8–80.9)Co–(8.9–11.2)Al–(7.8–10.4)W–(0.5–0.9)Ta. No Y atoms are observed in these two phases. Ta is found to divide γ′-Co_3(Al, W) phase rather than γ-Co_{SS} phase. These compositions for γ′ and γ phases are consistent with those from Y-free Co–9Al–9W–2Ta–0.02B alloy aged at 800 °C for 100 h [20]. Table 2 also summarizes the compositions of the phases at grain boundaries of the four aged alloys. Y is found to fully segregate in dark or gray area of grain boundaries (arrows A in Figs. 2a″–d″, 3a′–d′), and as nominal Y content increases, Y concentration in dark or gray area monolithically increases. A comparison of the compositions of dark or gray area and γ-Co_{SS} phase in grain interiors shows that the dark or gray area possesses a

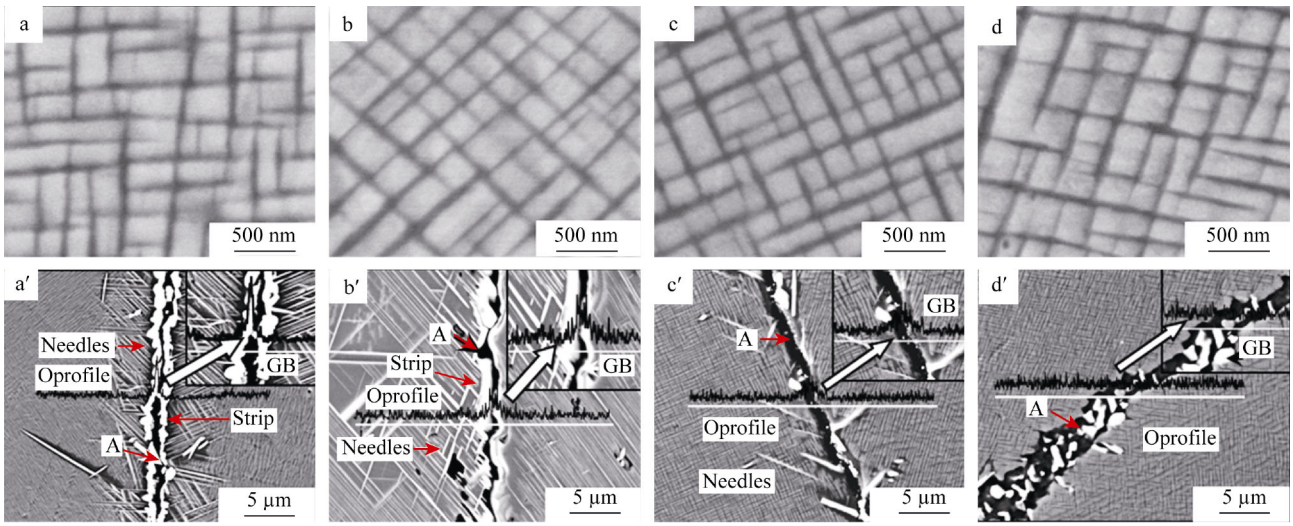

Fig. 3 SEM images of **a–d** grain interiors and **a′–d′** grain boundary of alloys aged at 900 °C for 150 h (insets in **a′–d′** being enlarged O profiles obtained by EDS scanning across grain boundaries, where white lines across grain boundary (GB) are EDS scanning position: **a, a′** 0.01Y alloy, **b, b′** 0.05Y alloy, **c, c′** 0.10Y alloy, and **d, d′** 0.20Y alloy

little higher Co and a lower Al + W + Ta concentration than γ-Co_{SS} phase, forecasting the creation of a γ-Co_{SS} structure from the dark or gray area of grain boundaries according to Co–Al–W ternary diagram [21]. γ-Co_{SS} phase at grain boundary possesses an Al content higher than W content by 50%–100%. This difference between Al and W contents is significantly larger than that between Al and W contents for γ-Co_{SS} phase at grain interiors (Table 2). Therefore, at grain boundaries, W may be exacerbated from γ-Co_{SS} phase, i.e., a decreasing W solubility in γ-Co_{SS} phase, resulting in the precipitation of strip, needle, and particle at grain boundaries.

From Table 2, it can be observed that the compositions of bright phases at grain boundaries, either stripes or particles, are not visibly influenced by aging time and nominal Y content. Therefore, these bright phases may be considered to be an identical phase. The average composition of these bright phases of the four aged alloys is determined to fall in the range of (70.1–73.6)Co–(4.7–6.8)Al–(14.2–17.5)W–(5.8–7.7)Ta. In these bright phases, W concentration is greater than Al + Ta concentration and the atomic ratio of Co to Al + W + Ta is close to 3:1, which is the stoichiometric ratio of a κ-Co_3W binary alloy. Thus, the bright phases in grain boundary may be primarily marked as the κ-Co_3(W) phase, where W may be partly replaced by Ta and Al.

An elemental comparison of compositional distribution across grain boundaries was carried out via EDX scan, as shown in Fig. 3a′–d′. Interestingly, 0.01Y, 0.05Y, and 0.10Y alloys exhibit an obvious O peak at grain boundaries (insets in Fig. 3a′–c′), qualitatively confirming a higher O concentration at grain boundaries than in grain interiors. However, O profiles at grain boundaries and grain interiors of 0.20Y alloy are almost even (inset in Fig. 3d′), revealing more Y segregation that excludes O from grain boundaries, resulting in cleaner grain boundaries.

To further identify the structures of needlelike precipitates at grain boundaries, a TEM bright field image and a typical SAED pattern of γ/γ′/needle microstructure were extracted from the 0.01Y alloy aged for 150 h, as shown in Fig. 4. Using the inserted beam [0 1 1] $L1_2$, two sets of diffraction patterns are obtained from γ/γ′/needle microstructure (denoted by a circle in Fig. 4a). One diffraction pattern in Fig. 4b (marked by larger and thickened circles) is the same as that shown in inset in Fig. 2a′ and is identified to originate from γ′ and γ coherent microstructure background. Using the same insert beam, a set of weak diffraction spots arranged in a rectangle are observed besides those from γ/γ′ background, which are observed as smaller dots marked by smaller circles in Fig. 4b. The weak rectangular diffraction pattern is believed to come from needlelike precipitate and is confirmed to be a DO_{19} structure. The fact that the needles grow from κ-Co_3(W) strips (Fig. 3a′, b′) and have a composition of 71.5Co–4.9Al–16.5W–7.1Ta determined by EDX which is the same as that of κ-Co_3(W) strips (Table 2), confirming that they are also composed of κ-Co_3(W) phase. By combining Fig. 4b and SAED patterns taken from various directions, it can be observed that κ-Co_3(W) needle exhibits a singular orientation relationship (OR) with respect to γ′ phase: $(0\,0\,0\,1)_{\kappa}//(1\,1\,\bar{1})_{\gamma}[1\,\bar{2}\,1\,0]_{\kappa}//[0\,1\,1]_{\gamma'}$.

The typical distributions of grain boundary misorientation angles for the four samples aged at 900 °C for 150 h are shown in Fig. 5. Low-angle (misorientation angle <15° [22]) grain boundaries (LABs) make up more than half of

Table 2 Compositions of constituent phases in grain interior (GI) and at grain boundary (GB) of four alloys aged at 900 °C and 1000 °C for 50 and 150 h (at%)

Alloys	Positions	Phases	Co		Al		W		Ta		Y	
			900 °C	1000 °C	900 °C	1000 °C	900 °C	1000 °C	900 °C	1000 °C	900 °C	1000 °C
0.01Y(50 h)	GB	γ	82.9	80.2	9.6	11.9	6.5	7.2	0.8	0.5	0.2	0.2
		$Co_3(W)$	70.1	72.8	4.7	5.2	17.5	15.3	7.7	6.7	–	–
	GI	γ′	76.5	75.1	10.6	10.9	9.8	10.8	3.1	3.2	–	–
		γ	80.6	79.2	9.9	9.9	8.9	10.3	0.6	0.6	–	–
0.05Y(50 h)	GB	γ	81.7	81.1	10.3	10.1	6.7	7.2	0.5	0.7	0.8	0.9
		$Co_3(W)$	71.1	73.3	6.8	6.3	16.2	14.3	5.9	6.1	–	–
	GI	γ′	75.2	74.7	10.9	11.3	11.1	11.1	2.8	2.9	–	–
		γ	80.1	79.4	10.2	10.7	8.9	9.2	0.8	0.7	–	–
0.10Y(50 h)	GB	γ	81.8	81.9	9.4	9.7	6.3	5.8	0.8	0.7	1.7	1.9
		$Co_3(W)$	72.5	74.6	5.9	6.1	15.4	11.6	6.2	7.7	–	–
	GI	γ′	75.8	73.7	11.5	11.6	10.5	11.3	2.2	3.4	–	–
		γ	78.8	78.4	9.9	11.9	10.4	8.9	0.9	0.8	–	–
0.20Y(50 h)	GB	γ	81.1	80.3	9.2	10.6	6.5	6.3	0.7	0.6	2.5	2.2
		$Co_3(W)$	70.6	71.9	6.8	6.4	15.2	14.2	7.4	7.5	–	–
	GI	γ′	74.5	74.1	10.7	11.9	11.9	10.9	2.9	3.1	–	–
		γ	79.6	78.6	8.9	10.5	10.9	10.3	0.6	0.6	–	–
0.01Y(150 h)	GB	γ	83.5	80.9	10.6	11.1	5.1	6.7	0.6	1.1	0.2	0.2
		$Co_3(W)$	71.9	69.4	5.3	7.3	15.1	15.4	7.7	7.9	–	–
	GI	γ′	75.9	76.9	11.3	11.2	10.2	9.4	2.6	2.5	–	–
		γ	80.6	79.5	10.1	10.3	8.6	9.5	0.7	0.7	–	–
0.05Y(150 h)	GB	γ	82.1	79.9	10.8	11.8	5.4	6.9	0.6	0.6	1.1	0.8
		$Co_3(W)$	71.1	74.1	6.8	5.7	16.2	14.6	5.9	5.6	–	–
	GI	γ′	75.5	74.9	11.4	11.3	9.8	10.9	3.3	2.9	–	–
		γ	80.9	78.9	10.7	10.6	7.8	9.8	0.6	0.7	–	–
0.10Y(150 h)	GB	γ	80.8	80.8	10.9	10.6	5.9	6.1	0.8	0.8	1.6	1.7
		$Co_3(W)$	72.7	72.9	6.6	5.5	14.9	16.3	5.8	5.3	–	–
	GI	γ′	74.6	75.4	11.9	11.7	10.7	10.6	2.8	2.3	–	–
		γ	79.3	79.7	11.2	10.1	8.7	9.1	0.8	1.1	–	–
0.20Y (150 h)	GB	γ	80.6	79.9	10.3	10.1	6.3	6.8	0.7	1.1	2.1	2.1
		$Co_3(W)$	73.6	69.6	5.1	8.7	14.2	14.5	7.1	7.2	–	–
	GI	γ′	76.9	77.4	10.5	10.9	10.1	10.1	2.5	1.6	–	–
		γ	79.9	79.1	10.3	10.6	9.3	9.8	0.5	0.5	–	–

the boundaries with the other grain boundaries having misorientation angles of 15°–60°, suggesting a Σ1-dominated grain boundary character distribution (GBCD) [23]. The frequency of LABs counted is approximately 59% for 0.01Y and 0.05Y alloys, and it increases to 70% for 0.10Y and 0.20Y alloys.

3.3 Microstructures of four alloys aged at 1000 °C

In grain interiors of samples aged at 1000 °C for 50 h, a coarsen γ/γ′ coherent microstructure is observed (Fig. 6a–d), and the content of stripe and needle precipitates decreases with Y content increasing to 0.10 at% (Fig. 6a′–c′). 0.20Y alloy still exhibits bright particles at grain boundaries (Fig. 6d′). As aging time increases to 150 h, γ/γ′ coherent microstructure in grain interiors (Fig. 7a–d) and precipitates at grain boundaries (Fig. 7a′–d′) further coarsen compared to the corresponding alloys aged for 50 h. In addition, a γ′-depletion zone near grain boundaries of 0.01Y, 0.05Y, and 0.10Y alloys forms. Similarly, a Σ1-dominated GBCD is also found in the four alloys aged at 1000 °C for 150 h. The frequency of LABs is about 55% for 0.01Y and 0.05Y alloys, 63% for 0.10Y alloy, and 69% for 0.20Y alloy.

Table 2 also shows phase compositions of the alloys aged at 1000 °C for various time. The bright strips and particles at grain boundaries of each aged alloy have a similar composition that is consistent with the bright phase in the four alloys aged at 900 °C (Table 2), in

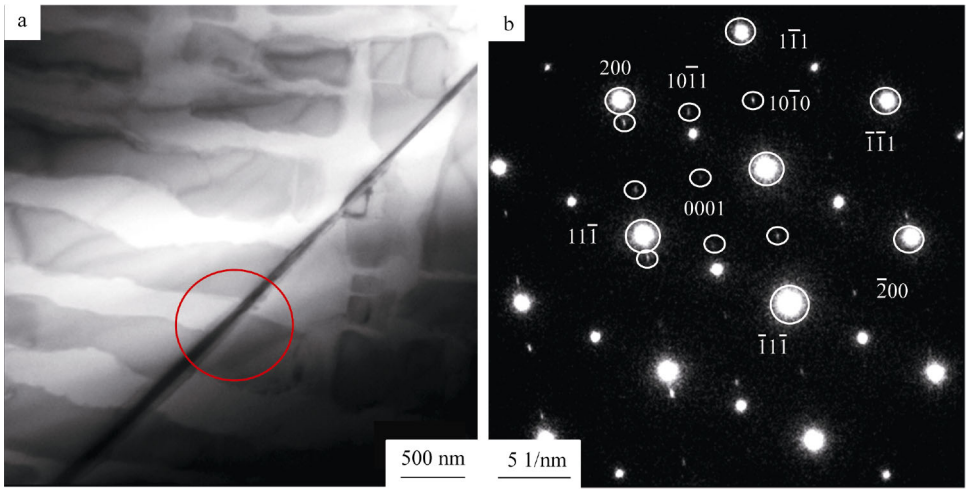

Fig. 4 TEM bright field image of 0.01Y alloy aged at 900 °C for 150 h and SAED pattern of γ/γ′/needlelike precipitate microstructures near grain boundary with inset beam [011]$L1_2$ phase: **a** TEM bright field image and **b** SAED pattern

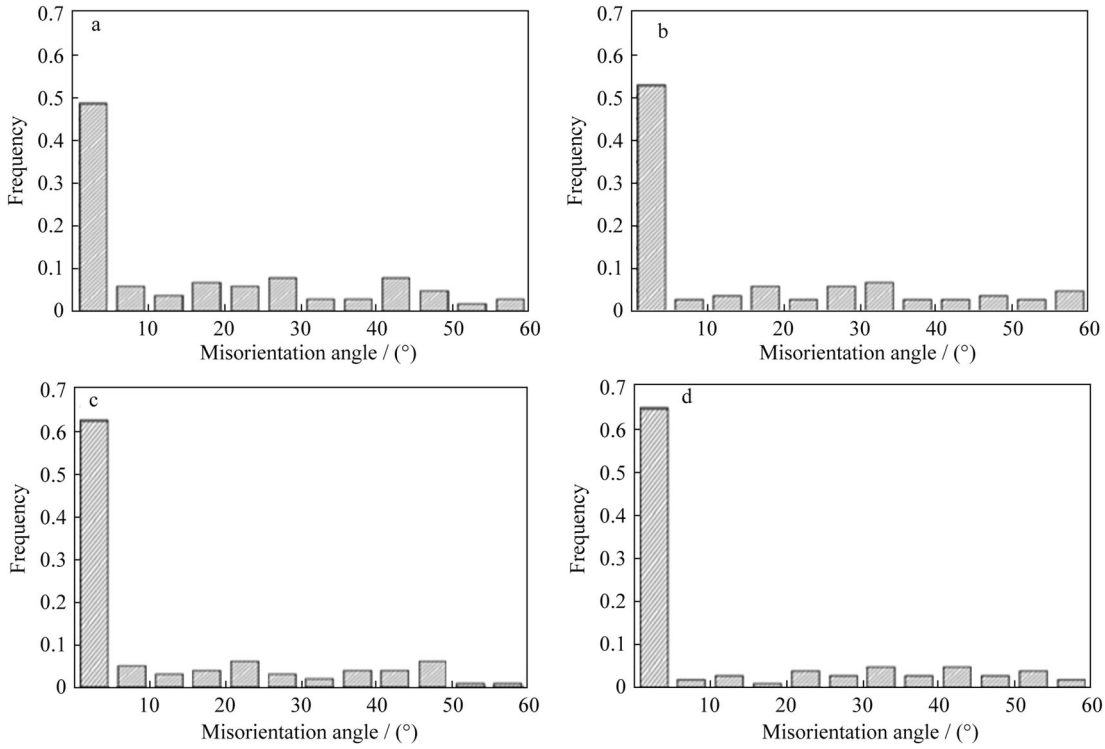

Fig. 5 Grain boundary misorientations of alloys aged at 900 °C for 150 h as a function of nominal Y content: **a** 0.01Y alloy, **b** 0.05Y alloy, **c** 0.10Y alloy, and **d** 0.20Y alloy

which no Y is detected. Y has been determined to solidify in gray area at grain boundaries, revealing the same segregation behavior of Y as observed in alloys aged at 900 °C, as shown in Table 2. From Table 2, it can be confirmed that intermetallic κ-Co_3(W) phase and solid-solution γ-Co_{SS} phase segregated with Y exist at grain boundaries of the aged Co–Al–W-based alloys, which is independent of nominal Y content and aging temperature and time.

4 Discussion

4.1 Microstructural evolution of Co–9Al–9W–2Ta–0.02B–(0.01–0.20)Y alloys

In this investigation, the phase composition of the aged Co–9Al–9W–2Ta–0.02B alloy doped with Y is independent of aging temperature and time. γ/γ′ coherent microstructure in grain interiors and γ/κ-

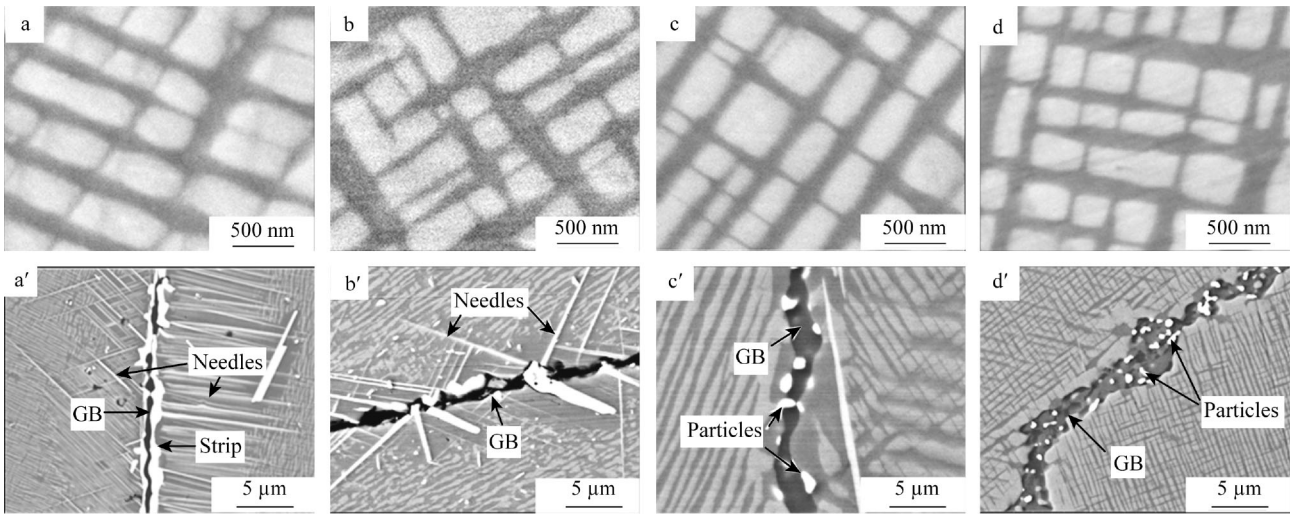

Fig. 6 SEM images of **a–d** grain interiors and **a′–d′** grain boundary of four alloys aged at 1000 °C for 50 h: **a, a′** 0.01Y alloy, **b, b′** 0.05Y alloy, **c, c′** 0.10Y alloy, and **d, d′** 0.20Y alloy

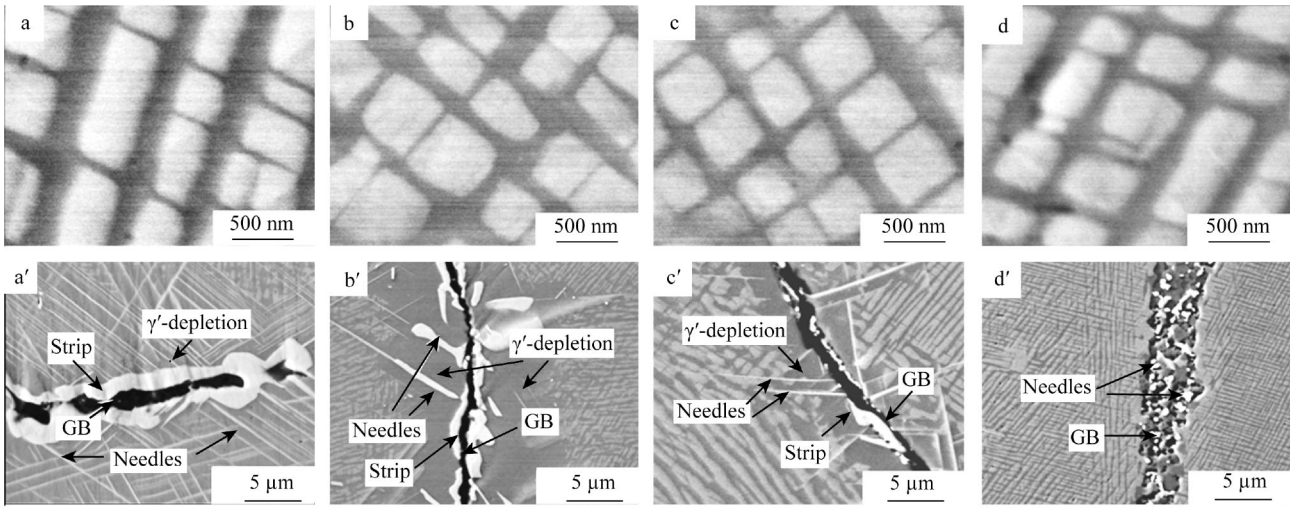

Fig. 7 SEM images of **a–d** grain interiors and **a′–d′** grain boundary morphologies of four alloys aged at 1000 °C for 150 h: **a, a′** 0.01Y alloy, **b, b′** 0.05Y alloy, **c, c′** 0.10Y alloy, and **d, d′** 0.20Y alloy

$Co_3(W)$ precipitates at grain boundaries are clearly identified. Table 3 summaries the sizes and area fractions (*f*) of the phases as a function of aging temperature and time, in which the standard deviation (SD, in nm) of the phase size is still listed. In general, the statistic size of γ phase shows a tightly increasing relationship with aging temperature and time, whereas the area fraction of γ phase seems to be independent of aging parameters, and it is (76 ± 3)%. When aged at 900 °C, for example, the size of most γ′ phases in 0.01Y alloy increases from 210 to 231 nm with an increase in aging time from 50 to 150 h. However, when the aging condition changes from 900 °C/150 h to 1000 °C/150 h, the size of most γ′ phases in 0.20Y alloy increases from 244 to 364 nm. The aging temperature is the key parameter for the growth of γ′ phase.

Y additions do not visibly change γ/γ′ coherent microstructure in grain interiors, including the size, area fraction and squareness of γ′ phase at a given aging temperature and time. However, Y fully segregates at grain boundaries, leading to significant metallurgical changes in grain boundary morphologies. The metallurgical changes concluded from Figs. 3, 5, and 7 include the following three aspects. (1) The precipitation of strip and needle κ-$Co_3(W)$ phase at grain boundaries is significantly restrained by the addition of more Y. As observed from Figs. 3a′, 7a′, 0.01Y alloy exhibits thick κ-$Co_3(W)$ strips and dense κ-$Co_3(W)$ needles, but few are observed when Y content increases to 0.10 at% (Figs. 3c′, 7c′), and the strip and needle phase completely disappear in 0.20Y alloy (Figs. 3d′, 7d′). (2) Grain boundaries are cleaned up by the

Table 3 Sizes and area fractions (*f*) of γ′ phase in four alloys dependent on aging temperatures and time

Aging conditions	0.01Y			0.05Y			0.10Y			0.20Y		
	Size/nm	SD/nm	*f*/%	Size/nm	SD/nm	*f*/%	Size/nm	SD/nm	*f*/%	Size/nm	SD/nm	*f*/%
900 °C/50 h	210	33	78	203	21	75	220	31	73	198	17	73
900 °C/150 h	231	41	79	247	32	75	239	25	78	244	23	78
1000 °C/50 h	290	51	76	281	48	74	296	55	75	282	44	74
1000 °C/150 h	374	49	78	382	46	78	370	56	74	364	67	75

exclusion of impurity element O by a higher nominal Y content (Fig. 3a′–d′). (3) The amount of LABs, i.e., Σ1 grain boundaries, increases with nominal Y content (Fig. 5). Referring to the phase compositions in Table 2, it can be deduced that κ-Co_3(W) precipitates at grain boundaries because W which is necessary for the formation of γ′-Co_3(Al, W) phase is greatly excluded from γ-Co_{SS} phase of grain boundaries. Subsequently, the extra W atoms precipitate in the form of γ-Co_3(W) phase rather than γ′-Co_3(Al, W) phase. In addition, W may also diffuse from γ′-Co_3(Al, W) phase in matrix to grain boundaries and result in high W concentration in grain boundaries, leaving a γ′-depletion zone near grain boundaries (Fig. 7a′–c′). This may be due to a combined action of defect effect of grain boundaries and Y segregation. Then, γ-Co_{SS} phase which has a lower W content than γ-Co_{SS} phase in grain interiors remains at grain boundaries besides κ-Co_3(W) precipitates. The aforementioned metallurgical evolution of grain boundary morphologies caused by Y addition undoubtedly governs the bulk mechanical response, especially for the case of tensile stress, as the intergranular fracture in these Co–Al–W-based γ/γ′ coherent microstructures at room and high temperatures has been recognized [6, 18, 19], which also occurs in polycrystalline γ′-Ni_3Al alloys [23].

4.2 Potential of Co–Al–W-based alloys as high-temperature structural materials

In particular, when the polycrystalline alloys are maintained at high temperature, grain boundary precipitation, segregation of the impurities and sliding and migration preferentially occur and may affect the fracture processes, such as adopting an intergranular or transgranular mode. Estimating the microstructure may provide optimized stable γ/γ′ coherent microstructure (without needles or stripes precipitating along grain boundary), aging parameters and nominal Y content. Currently, the majority of progress in determining mechanical response of Co–Al–W-based alloys has been performed using compressive loading [5–7, 11, 12], and recently some tensile creep behavior of single-crystal Co–Al–W-based alloys has been investigated [14, 24].Until now, the positive contribution of the γ′ phase [6–8] or intermetallic precipitates at grain boundaries [11, 12] on the bulk strength and ductility of the polycrystalline Co–Al–W-based alloys in the compressed state have been confirmed. However, its role under the uniaxial tensile conditions has not been fully recognized.

Earlier work [18] found that for γ/γ′-Co_3(Al, W) microstructure free from needle precipitates, slip bends were observed on aligned γ and γ′ phases and the alloy failed in a dimple mode [18, 19] at room temperature, with a tensile elongation of larger than 9%. However, the polycrystalline Co–Al–W–Ta–Mo–B alloys with needle-like precipitates presented at grain boundaries failed along precipitate area with tensile elongation of <1%, and the coherent γ/γ′ microstructure also possessed an anomalously low elongation of ~3.3% at 600–800 °C [19] for the intergranular cleavage fracture. These low tensile elongations and ductility are identified to be caused by grain boundary morphologies.

As expected, a large fraction of strengthening γ′ phases (73%–79%) (Table 3) is a guarantee of better tensile strength or creep resistance in γ/γ′-Co_3(Al, W) microstructure at high temperatures, which has been proved in Ni-based superalloys [2, 3], even though increasing the size of γ′ may decrease tensile strength to some extent when the aging temperature is high. However, the needle and strip intermetallics precipitated along grain boundaries are certain to be harmful to tensile ductility. It is recognized that for 0.01Y and 0.05Y alloys, significant numbers of needles and strips may dissever matrix and grain boundaries or cause significant stress concentrations at grain boundaries, resulting in premature failure and poor tensile ductility at room and high temperatures via an intergranular cleavage process. Decreasing aging temperature to 800 °C may restrain precipitation of needles and strips [18]. Subsequently, the temperature endurance capacity of these alloys is limited to low aging temperature. After aging at 1000 °C, 0.10Y alloy possesses few needle and particle precipitates at grain boundaries, and only fine particles scattered at grain boundaries are found in 0.20Y alloy. These morphologies of intermetallic precipitates avoid the cutting and stress concentration effects at grain

boundaries and intergranular cleavage. Therefore, better tensile elongation is expected in these two alloys.

Finally, the intergranular cleavage of polycrystalline intermetallics is also found to depend on GBCD and the impurities at the grain boundaries [25–28]. The pioneering works in $L1_2$–Ni_3Al [29] found that only Σ1 low-angle grain boundaries [22] and symmetrical Σ3 twin boundaries are particularly resistant to intergranular fracture. Therefore, the fracture strength or the ductility of intergranularly brittle intermetallics may be increased only by increasing the content of low-angle Σ1 and possibly Σ3 boundaries in $L1_2$ and B2 compounds [22]. Apparently, increasing nominal Y content introduces more LABs (Fig. 5) in Co–Al–W–Ta–Mo–B alloys and reduces impurity O segregation at grain boundaries (Fig. 3a′–d′). Both of these actions are believed to be beneficial to the strength of grain boundaries and the elongation of bulk γ/γ′-Co_3(Al, W) coherent microstructure at room and high temperatures by restraining instances of intergranular fracture. Nevertheless, effect of complex interaction between dislocation and GBCD on failure mode and tensile ductility should be considered, due to that the slip plane {0 0 1} is active at the anomalous flow stress temperatures [5, 6]. Currently, a comprehensive evaluation of microstructural stability and mechanical behavior at room and high temperatures under uniaxial tension as a function of Y content is being conducted, which will provide optimized Co–Al–W–Ta–Mo–B–Y alloys.

5 Conclusion

The microstructure of as-cast 0.01-0.20Y alloys consists of a γ/γ′ matrix and Co_3(Ta, Me) dots or short chins. Co_3(Ta, Me) phase is scattered on the interstices of dendritic-like matrix and Y fully segregates in Co_3(Ta, Me) phase. After aging at 900 and 1000 °C for 50 and 150 h, Co_3(Ta, Me) phase in as-cast alloys disappears. The microstructures of 0.01-0.20Y alloys in grain interiors are composed of γ-Co_{SS} matrix and nanoscale cuboidal γ′-Co_3(Al, W) precipitates. γ-Co_{SS} and the γ′-Co_3(Al, W) phases cohere with each other. The size of cuboidal γ′-Co_3(Al, W) increases monotonically with aging temperature, and γ′-Co_3(Al, W) content of the four aged samples is (76 ± 3)% for the aging parameters investigated in this work. In the aged samples, κ-Co_3(W) phase precipitates at grain boundaries. Y fully segregates at grain boundaries and significantly changes κ-Co_3(W) precipitate morphologies at grain boundaries. An increasing amount of Y suppresses the formation of κ-Co_3(W) stripe precipitates at grain boundaries and the growth of κ-Co_3(W) needles from grain boundaries or κ-Co_3(W) stripes toward grain interiors. This is instead of the fine κ-Co_3(W) particles being scattered at grain boundaries. The four aged alloys have a Σ1-dominated grain boundary character distribution (GBCD). Increasing Y content leads to an increase in the proportion of low-angle grain boundaries (Σ1) and restrains the tendency of O to segregate at grain boundaries.

Acknowledgements This work was financially supported by the National Natural Science Foundation of China (No. 51471014).

References

[1] Sullivan CP. Cobalt Base Superalloys, Cobalt Monograph Series. Brussels: Centre d'information du Cobalt; 1970. 116.
[2] Pollock TM, Argon AS. Creep resistance of CMSX-3 nickel base superalloy single crystals. Acta Metall Mater. 1992;40(1):1.
[3] Zhang JX, Wang JC, Harada H, Koizumi Y. The effect of lattice misfit on the dislocation motion in superalloys during high-temperature low-stress creep. Acta Mater. 2005;53(17):4623.
[4] Sato J, Omori T, Oikawa K, Ohnuma I, Kainuma R, Ishida K. Cobalt-base high-temperature alloys. Science. 2006;312(5770):90.
[5] Shinagawa K, Omori T, Oikawa K, Kainuma R, Ishida K. Ductility enhancement by boron addition in Co–Al–W high-temperature alloys. Scr Mater. 2009;61(6):612.
[6] Suzuki A, Denolf GC, Pollock TM. Flow stress anomalies in γ/γ′ two-phase Co–Al–W-base alloys. Scr Mater. 2007;56(5):385.
[7] Suzuki A, Pollock TM. High-temperature strength and deformation of γ/γ′ two-phase Co–Al–W-base alloys. Acta Mater. 2008;56(5):1288.
[8] Jiang C. First-principles study of Co-3(Al, W) alloys using special quasi-random structures. Scr Mater. 2008;59(8):1075.
[9] Klein L, Bauer A, Neumeier S, Göken M, Virtanen S. High temperature oxidation of γ/γ′-strengthened Co-base superalloys. Corros Sci. 2011;53(5):2027.
[10] Ooshima M, Tanaka K, Okamoto NL, Kishida K, Inui H. Effects of quaternary alloying elements on the γ′ solvus temperature of Co–Al–W based alloys with fcc/L1(2) two-phase microstructures. J Alloys Compd. 2010;508(1):71.
[11] Bauer A, Neumeier S, Pyczak F, Göken M. Microstructure and creep strength of different γ/γ′-strengthened Co-base superalloy variants. Scr Mater. 2010;63(12):1197.
[12] Bauer A, Neumeier S, Pyczak F, Singer RF, Göken M. Creep properties of different γ′-strengthened Co-base superalloys. Mater Sci Eng A. 2012;550(7):333.
[13] Xue F, Zhou HJ, Ding XF, Wang ML, Feng Q. Improved high temperature γ′ stability of Co–Al–W-base alloys containing Ti and Ta. Mater Lett. 2013;112(12):215.
[14] Shi L, Yu JJ, Cui CY, Sun XF. Effect of Ta additions on microstructure and mechanical properties of a single-crystal Co–Al–W-base alloy. Mater Lett. 2015;149(6):58.
[15] Paidar V, Pope DP, Vitek V. A theory of the anomalous yield behavior in L1(2) ordered alloys. Acta Metall. 1984;32(3):435.
[16] Yamaguchi M, Umakoshi Y. The deformation of intermetallic superlattice compounds. Prog Mater Sci. 1990;34(9):1.
[17] Okamoto NL, Oohashi T, Adachi H, Kishida K, Inui H, Veyssière P. Plastic deformation of polycrystals of Co-3(Al, W) with the L1(2) structure. Philos Mag. 2011;91(28):3667.
[18] Feng G, Li H, Li SS, Sha JB. Effect of Mo additions on microstructure and tensile behavior of a Co–Al–W–Ta–B alloy at room temperature. Scr Mater. 2012;67(5):499.
[19] Zhong F, Li SS, Sha JB. Tensile behaviour of Co–Al–W–Ta–B–Mo alloys with a coherent γ/γ′ microstructure at room and high temperatures. Mater Sci Eng A. 2015;637(6):175.

[20] Shinagawa K, Chinen H, Omori T, Oikawa K, Ohnuma I, Ishida K, Kainuma R. Phase equilibria and thermodynamic calculation of the Co–Ta binary system. Intermetallics. 2014;49(6):87.
[21] Kobayashi S, Tsukamoto Y, Takasugi T, Chinen H, Omori T, Ishida K, Zaefferer S. Determination of phase equilibria in the Co-rich Co–Al–W ternary system with a diffusion-couple technique. Intermetallics. 2009;17(12):1085.
[22] Bystrzycki J, Varin TA, Nowell M, Kurzydlowski KJ. Grain boundary character distribution in B2 intermetallics. Intermetallics. 2000;8(9–11):1049.
[23] Takeyama M, Liu CT. Effects of grain size and test temperature on ductility and fracture behavior of a B-doped Ni_3Al alloy. Acta Metall. 1998;36(5):1241.
[24] Titus MS, Mottura A, Viswanathan GB, Suzuki A, Mills MJ, Pollock TM. High resolution energy dispersive spectroscop mapping of planar defects in L1(2)-containing Co-base superalloys. Acta Mater. 2015;89(50):423.
[25] Kaneno Y, Takasugi T. Grain-boundary character distribution in recrystallized L1(2) ordered intermetallic alloys. Metall Mater Trans A. 2003;34A(11):2429.
[26] Kim T, Hong KT, Lee KS. The relationship between the fracture toughness and grain boundary character distribution in polycrystalline NiAl. Intermetallics. 2003;11(1):33.
[27] Watanabe T, Tsurekawa S. The control of brittleness and development of desirable mechanical properties in polycrystalline systems by grain boundary engineering. Acta Mater. 1999;47(15):4171.
[28] Alexandreanu B, Sencer BH, Thaveeprungsriporn V, Was GS. The effect of grain boundary character distribution on the high temperature deformation behavior of Ni–16Cr–9Fe alloys. Acta Mater. 2003;51(13):3831.
[29] Hanada S, Ogura T, Watanabe S, Izumi O, Masumoto T. Application of the selected area channeling pattern method to the study of intergranular fracture in Ni_3Al. Acta Metall. 1986;34(1):13.